Soft Matter

PAPER

View Article Online
View Journal | View Issue

Published on 10 January 2018. Downloaded by National Synchrotron Radiation Research on 1/21/2019 4:00:38 AM.

Check for updates

Cite this: *Soft Matter*, 2018, **14**, 1270

PBTTT-C_{16} sol–gel transition by hierarchical colloidal bridging†

Han-Liou Yi and Chi-Chung Hua *

A versatile conjugated polymer, poly(2,5-bis(3-hexadecyllthiophen-2-yl)thieno[3,2-*b*]thiophene) (pBTTT-C_{16}, with M_w = 61 309 g mol^{-1}), in a relatively good solvent (chlorobenzene, CB) medium is shown to produce gels through hierarchical colloidal bridging. Multiscale static/dynamic light and X-ray scattering analysis schemes along with complementary microscopy imaging techniques clearly reveal that upon cooling from the solution state at 80 °C to various gelation temperatures (5, 10, and 15 °C), rod-like colloidal pBTTT-C_{16} aggregates morph into spherical ones, triggering hierarchical colloid formation and bridging that eventually turn the solution into a gel after about one-day aging. A certain fraction of primal packing units—spherical gelators (~1 nm in mean radius)—constitute the spherical building particles (~10 nm) noted above, which in turn constitute loose-packing aggregate clusters (~300 nm) in the sol state. As gelation proceeds, the aggregate cluster interiors tighten substantially, and micrometer-sized clusters (~3 μm) formed by them begin to take shape and further interconnect to form the gel network (mean porosity size ~240 nm and spatial inhomogeneity length ~20 μm). Rheological measurements and kinetic analysis reveal that the gelation temperature can also have a notable impact on gel microstructure, gelation rate, and mechanical strength, resulting in, for instance, a prominently nonergodic and porous structure for the soft gel incubated at a higher temperature T = 15 °C. The ac conductivity exhibits a notable upturn near pBTTT-C_{16}/CB gelation, well above those achieved by the counterpart pBTTT-C_{14} solutions, which, in interesting contrast, cannot be brought to the gel phase under similar experimental conditions.

Received 20th December 2017,
Accepted 10th January 2018

DOI: 10.1039/c7sm02493b

rsc.li/soft-matter-journal

1. Introduction

Conjugated polymers are versatile materials due to their excellent and tunable optical and electronic properties for a wide range of applications with organic photovoltaic devices (OPVs),[1,2] organic light-emitting diodes (OLEDs),[3,4] organic thin-film transistors (OTFTs),[5,6] and organic sensors.[7,8] High performances of polymer-based electronic devices usually require properly controlled nanoscale/mesoscale structural and morphological features. Among the attractive routes to fulfilling this goal is to capitalize on the gel phase of conjugated polymers, owing to the unique three-dimensional (3-D) structural order that is especially advantageous for charge/heat transports in addition to improved mechanical strength.[9–31] In practice, manipulating the self-assembly behavior and aggregation state has been elucidated to help optimize the structural features of conjugated polymer gels for electronic applications.[9–15,17,18] With changing polymer attributes and preparation/processing conditions, however, precise control over the properties of conjugated polymer gels remains a notably challenging task, as may be perceived from the following paragraph highlighting their diverse features in recent literature.

To date, gel formation has been reported and investigated in some detail only for a limited number of conjugated polymers, including poly(3-alkyl-thiophene) (P3ATs),[10,11,13,14,16,17,20] poly(9,9-dialkyl fluorene) (PFs),[15,21–25] poly(vinylene phenylene) (PVPs),[26–28] among others.[9,18,29] Poly(9,9-dioctylfluorenyl-2,7-diyl) (PFO) was found to crystallize into sheet-like structures or aggregates, which later agglomerate into ribbon-like structures allowing for the eventual formation of thermoreversible gels.[23] In contrast, poly(3-hexylthiophene) (P3HT) was known to develop fiber networks by utilizing the coil-to-rod transition or interchain π–π stacking.[12,30,31] The amorphous conjugated polymer poly[2-methoxy-5-(2′-ethylhexyloxy)-1,4-phenylenevinylene] (MEH-PPV) has recently been shown to capitalize on colloidal aggregates in solution and, upon reaching the gelation temperature in a hybrid–solvent medium, form 3-D interconnected colloidal gels.[26] Clearly, there exists little, if any, resemblance between the three types of polymer gels above.

Due to their high charge-carrier mobility[32–36] and good oxidative stability[32] for applications in OPVs[37,38] and OTFTs,[39] poly(2,5-bis(3-alkylthiophen-2-yl)thieno[3,2-*b*]thiophenes) (pBTTTs) have recently

Department of Chemical Engineering, National Chung Cheng University, Chiayi 62102, Taiwan. E-mail: chmcch@ccu.edu.tw

† Electronic supplementary information (ESI) available. See DOI: 10.1039/c7sm02493b

This journal is © The Royal Society of Chemistry 2018

Published on 10 January 2018. Downloaded by National Synchrotron Radiation Research on 1/21/2019 4:00:38 AM.

received much attention in a wide range of experimental[33,35,36,40,41] and theoretical[42–44] investigations. Among them, only poly(2,5-bis(3-hexadecylthiophen-2-yl)thieno[3,2-*b*]thiophene) (pBTTT-C_{16}) has been reported to produce gels[45] without knowing the underlying kinetics and structures. For instance, a recent study on the dilute solutions of poly(2,5-bis(3-tetradecylthiophene-2-yl)thieno[3,2-*b*]thiophenes) (pBTTT-C_{14}) observed no signs of physical gelation in two representative solvent media, toluene (T) and chlorobenzene (CB).[46] At a higher concentration (*i.e.*, 10 mg mL^{-1}), Fig. S1, ESI† presents the photographs showing further that the pBTTT-C_{14}/CB solution precipitates while the counterpart pBTTT-C_{16}/CB solution gels at 15 °C. Because we have observed distinct gelation mechanisms and structural features in CB for pBTTT-C_{16} of two different average molecular weights, the present report is focused on the results for the higher-molecular-weight sample, designated as Hw-pBTTT-C_{16}. Multiscale dynamic/structural features and rheological properties of Hw-pBTTT-C_{16}/CB have been systematically revealed using a comprehensive combination of characterization and analysis schemes, which include depolarized/polarized dynamic light scattering (DDLS/DLS), static light/X-ray scattering (SALS/SLS/SAXS), and rheological, dielectric, and optical/electron microscopy (OM/EM) analysis schemes. The results suggest that Hw-pBTTT-C_{16}/CB may employ a peculiar pathway of hierarchical colloidal bridging to form gels. The structural, mechanical, and electronic properties all point to the versatile features of pBTTT-C_{16} solutions and gels in future optical/electronic applications.

2. Experimental methods

2.1 Materials and sample preparations

The Hw-pBTTT-C_{16} sample investigated herein, with an average molecular weight M_w = 61 309 g mol^{-1} and a polydispersity index PDI = 5.04 (see the chemical structure inserted in Fig. 1), was purchased from Luminescence Technology Corp. (Taiwan) and used without further purification. The solvent used to dissolve Hw-pBTTT-C_{16}, chlorobenzene (CB; Sigma-Aldrich, ≥99.5% in purity), was filtered through a 0.22 μm PVDF filter (Millipore Millex-GN) to remove dust. A benchmark Hw-pBTTT-C_{16} solution with a concentration of 10 mg mL^{-1} was prepared with the filtered solvent. To fully dissolve the polymer in CB, the sample solution was sonicated for 12 h at 80 °C,[45,46] whereby a transparent and homogeneous solution was obtained. As shown in Fig. S1, ESI,† the Hw-pBTTT-C_{16} solution may be brought to gel *via* short-term aging (within one day) at a low temperature (15 °C), and the gel structure may be largely disintegrated by heating back to 80 °C. The freshly prepared, heated solution was allowed to equilibrate for at least 2 h at 80 °C to minimize the effect of prior sonication, and then it was quickly transferred to the sample carriers for all subsequent measurements. Most measurements described below were conducted during a fast quenching from 80 °C to various gelation temperatures (5, 10, and 15 °C), when the sample was allowed to stand for 30 min prior to the experiment. Upon reaching the individual gelation temperature, the effects of aging time were closely monitored until the gel network ripened in about one day or even less.

2.2 Light scattering (SLS/DLS/DDLS) analysis

Light scattering (LS) measurements were performed on a laboratory-built apparatus as described elsewhere.[26,47] A 20 mW polarized diode laser (λ_0 = 785 nm; Omicron, LuxX® 785, Germany) was used as the incident light to avoid absorption of Hw-pBTTT-C_{16}/CB in the visible-light region, especially at a concentration as high as 10 mg mL^{-1}. A UV-vis spectrometer was utilized to confirm that Hw-pBTTT-C_{16}/CB shows negligible absorption at the incident light wavelength, as detailed in Section S2, ESI.† The effect of incident light intensity has also been scrutinized, ensuring that the data reported were unaffected by absorption and the consequent thermal-induced flow convection, as detailed in Section S3, ESI.† According to the last requirement, the laser power was

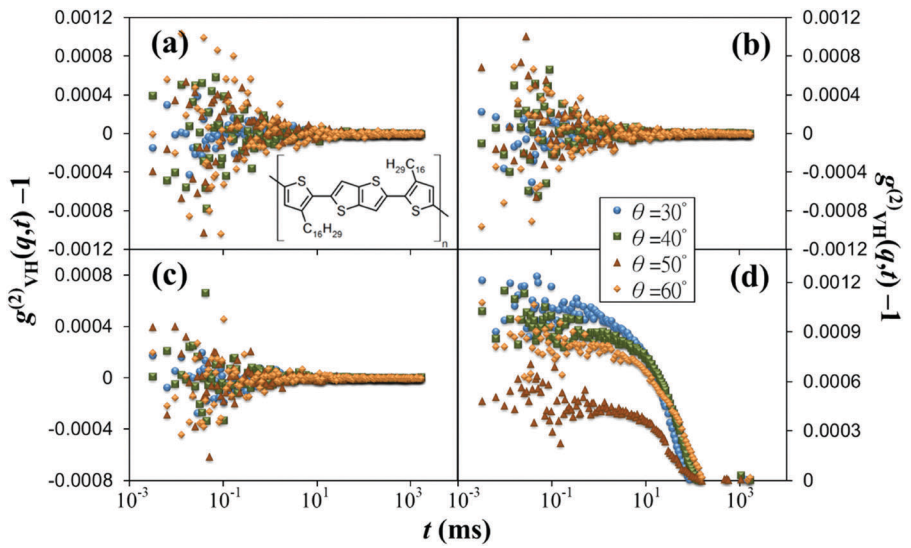

Fig. 1 Depolarized intensity correlation functions, $g_{VH}^{(2)}(q,t) - 1$, for Hw-pBTTT-C_{16}/CB solution (or sol) at four different temperatures: (a) 5, (b) 10, (c) 15, and (d) 80 °C, where the symbols represent the results from four different scattering angles. The chemical structure of pBTTT-C_{16} is inserted in (a).

Published on 10 January 2018. Downloaded by National Synchrotron Radiation Research on 1/21/2019 4:00:38 AM.

later attenuated to about 1 mW for most light scattering experiments. Moreover, ergodicity of the Hw-pBTTT-C_{16}/CB gels was assessed using a partial-heterodyne method, as detailed in Section S4, ESI.† Details of the SLS, DLS, and DDLS analysis schemes can be found in prior work.[46]

2.3 Small-angle scattering (SALS/SAXS) analysis

The apparatus for SALS measurements was described elsewhere.[26] SAXS measurements were carried out at beamline stations BL23A of Taiwan Light Source (TLS) and BL25A of Taiwan Photo Source (TPS) at the National Synchrotron Radiation Research Center (NSRRC) in Taiwan. The scattering X-ray covers a q-range of 0.04–3.0 nm^{-1}, with a 15 keV incident beam (wavelength λ_0 = 0.827 Å) and a sample-to-detector distance of 4714 mm. Unless mentioned otherwise, the measurements were conducted at the gelation temperature (5, 10, and 15 °C).

2.4 Dynamic modulus analysis

The TA Instruments DHR-2 stress-controlled rheometer was used with a cone-plate geometry (diameter = 40 mm, cone angle = 2°, and gap distance = 55 μm) and—for aging-time dependence measurements—with an aluminum double-gap cylinder geometry (the inner cup has a diameter of 30.2 mm, the inner and outer rotor diameters are 31.97 and 34.98 mm, respectively, and both the gaps have the same size of 0.95 mm after immersing the cylindrical rotor, which has a height of 53 mm). The above geometries were equipped with a Peltier temperature controller, which maintains the system temperature at 80 °C upon loading the fresh solution sample. To minimize the effect of solvent evaporation, a solvent trap was utilized during the entire measuring process. Detailed descriptions of the viscoelastic characterizations of the Hw-pBTTT-C_{16}/CB solution and gels can be found in Section S7, ESI.†

2.5 Optical/electron microscopy (OM/EM) analysis

OM images were taken using a conventional microscope (Olympus BX51, Japan) equipped with a high-resolution digital camera (Olympus DP22, Japan) and a laboratory-built heating/cooling temperature controller. The samples for OM characterization were prepared by casting the Hw-pBTTT-C_{16}/CB solution into a cell having a gap size of 2 mm, followed by cooling to the gelation temperature. To obtain more detailed information about the shape and dimension of Hw-pBTTT-C_{16}/CB aggregates, the sample solution was filtered through a copper grid coated with carbon film, which was placed on filter paper (ADVANTEC filter paper 1) to undergo natural drying at room temperature (for STEM and TEM imaging). The images of the resulting sample were taken in a transmission electron microscope (JEOL JEM-2010) at an acceleration voltage of 200 kV, as well as in a scanning electron microscope (Hitachi S4800-I) at an acceleration voltage of 15 kV. The same EM apparatus was utilized in both measurements.

2.6 Ac conductivity analysis

Measurements of ac conductivity were performed using a Solartron 1296 dielectric interface coupled to a Solartron 1260 frequency response analyzer, operating at a frequency of 2 kHz and a small voltage (200 mV) in the linear impedance region. The sample was placed between the parallel-plate electrodes (diameter = 25 mm and gap size = 0.2 mm) made of stainless steel and electrically insulated with machining ceramics, along with a laboratory-built temperature controller that achieves a heating rate of 4 °C min^{-1}.

3. Results and discussion

Chlorobenzene (CB) represents a relatively good solvent for pBTTT-C_n when compared with another close analogue, toluene,[48] and is especially good for spin-coating, for instance, due to its high boiling point. To foster gels in CB medium within a one-day period, the resulting Hw-pBTTT-C_{16}/CB sample needs to be brought to temperatures not higher than 15 °C, and lower temperatures were noted to expedite the entire gelation process. Fig. S1, ESI† provides the photographs showing the gelation of the 10 mg mL^{-1} Hw-pBTTT-C_{16}/CB solution after aging for 24 h at 15 °C; the gel has been confirmed to be stable (over a period >7 days) and thermally reversible.

3.1 General features of Hw-pBTTT-C_{16}/CB sol–gel transition

The DDLS analysis was first carried out to reveal the bulk features of Hw-pBTTT-C_{16}/CB aggregates; as the system temperature was steadily reduced, fresh solution at 80 °C underwent a sequence of "gelling" states at 5, 10, and 15 °C. The following comparisons are based on measurements conducted at the initial (sol) state, before sufficient time (about 16 h) had passed to bring the system to a real gel state. The depolarized intensity correlation function, $g^{(2)}_{VH}(q,t) - 1$, for the fresh solution at 80 °C exhibits a clearly discernible relaxation pattern (Fig. 1d), in contrast with the other low-temperature states that produce no discernible patterns within the experimental uncertainty. Interestingly, these DDLS features suggest that while the aggregates formed in the pristine solution at 80 °C are anisotropic (rod-like) in shape, they are basically isotropic (sphere-like) in the gelling state. This essential trend is corroborated by the STEM and TEM images shown in Fig. 2b and c, which compare the fast-drying thin-film morphologies produced from a fresh solution (at 80 °C) and a gelling sample (at 15 °C).

From a different perspective, Fig. 2a presents the typical SAXS profiles (for solution or sol). In the high-q region, the results reflect mainly the geometrical features of the primary building particles or aggregates (see later discussions). It can be seen that as the temperature drops from 80 °C (yellow squares) to various gelling temperatures, the scaling behavior in this region alters systematically from $I(q) \sim q^{-1}$ to $I(q) \sim q^{-4}$ corresponding to the rod-like and full-collapsed globular aggregates, respectively, and the trend may be reversed by raising the system temperature back to 80 °C. Intriguingly, these results indicate that gelation of Hw-pBTTT-C_{16}/CB requires not only the mutual bonding between chains or aggregates in the original solution, as is often observed for polymer and low-molecular-mass gelators,[49,50] but it also involves a fundamental change in aggregate shape before gelation may be triggered or proceed.

 This journal is © The Royal Society of Chemistry 2018

Published on 10 January 2018. Downloaded by National Synchrotron Radiation Research on 1/21/2019 4:00:38 AM.

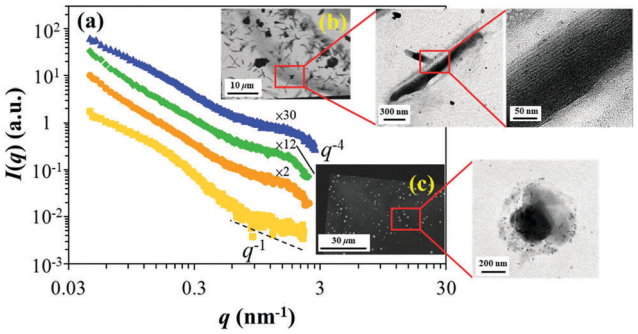

Fig. 2 (a) SAXS patterns for the solution (or sol) of Hw-pBTTT-C_{16}/CB, where the symbols represent the results at four different temperatures: 5 (blue triangles), 10 (green diamonds), 15 (orange spheres), and 80 °C (yellow squares). These curves, except for 80 °C, have been vertically shifted to facilitate the comparison; the STEM and TEM morphologies of the drop-cast thin films produced from the Hw-pBTTT-C_{16}/CB solution (or sol) at (b) 80 and (c) 15 °C are also shown.

3.2 Identification of the gel points and characterization of ac conductivities

The temperature dependence of dynamic modulus often serves to identify the so-called gel point. To facilitate the data comparison, Hw-pBTTT-C_{16}/CB gels incubated at three different temperatures (5, 10, and 15 °C) were left undisturbed for 24 h before the subsequent heating was carried out. Fig. 3 shows the dynamic modulus responses upon heating the Hw-pBTTT-C_{16}/CB gels described above. In general, the material remains solid-like at low temperatures with $G' > G''$, and it becomes liquid-like at high temperatures with $G' < G''$. Thus, the crossover point, $G' = G''$, is often referred to as the gelation temperature, T_{Gel}. It can be seen that this simple criterion results in some slight difference in T_{Gel}, which might be attributed to the disparity in the underlying gel structures that are further coupled to the heating history; see later discussions.

Another interesting feature is concerned with the comparison between the Hw-pBTTT-C_{16} and pBTTT-C_{14} solutions for the ac conductivity pertinent to their OTFT applications. Hw-pBTTT-C_{16}/CB can be seen to exhibit a notable upturn in ac conductivity near the gelation temperature, and, under similar experimental conditions, yield a considerably higher conductivity than the counterpart pBTTT-C_{14}/CB and pBTTT-C_{14}/T solutions. Despite the fact that the apparatus utilized prevents direct access to the Hw-pBTTT-C_{16}/CB gel at 15 °C, when the changes in ac conductivity are expected to be more prominent, the overall trend is consistent with early findings for P3HT,[10,11] whose gel phase showed a substantial enhancement in ac conductivity over the solution phase.

Fig. 4a–d presents the corresponding behavior of time-averaged scattering intensities, $\langle I \rangle_T$, at randomly selected positions (by rotating and lifting the sample cuvette) for the solution (T = 80 °C) and gel (T = 5, 10, and 15 °C) samples. These results are typical of solution (homogeneous) and gel (heterogeneous) samples. Fig. 4e presents the SAXS patterns for the three gel samples. While the high-q data reflect similar geometrical features for the building particles, the low-q data indicate varying large-scale microstructures that are consistent with the behaviors of $\langle I \rangle_T$ discussed below.

Using the partial heterodyne method described in early work,[26,51,52] $\langle I \rangle_T$ may be analyzed along with DLS data to retrieve $\langle I_d \rangle_T$, which represents the intrinsic part of $\langle I \rangle_T$ that is independent of the measuring position. The disparity between $\langle I_d \rangle_T$ and the ensemble-averaged $\langle I \rangle_E$ (see descriptions in Fig. 4) helps to reveal the degree of nonergodicity of a gel sample. Fig. 4a shows that $\langle I \rangle_E = \langle I_d \rangle_T$, as might be expected for a solution sample. For the gel samples shown in Fig. 4b–d, the disparity between $\langle I_d \rangle_T$ and $\langle I \rangle_E$ becomes more pronounced and increases with increased gelation temperature, suggesting a higher degree of heterogeneity for gels incubated at a higher temperature. Along with the SAXS profiles in Fig. 4e, it is clear that the gelation temperature primarily alters the spatial packing of (micrometer-sized) clusters. Another interesting feature is that $\langle I \rangle_E$ increases as the Hw-pBTTT-C_{16} solution (or sol) turns into a gel. Polymer gels often show similar behavior, as the isolated chains in solution are less capable of scattering light;[49,53–55] in contrast, colloidal gels[56] and gels formed by polymer microgels[51] typically exhibit the opposite trend because of the interferences of light scattered by spatially correlated particles—the so-called structure factor. As we discuss later, the Hw-pBTTT-C_{16}/CB gels bear no real resemblance to either case (*i.e.*, polymer or colloid), although the features above seem to resemble those of usual polymer gels. It is also worth noting that the extracted value of D (see the definition in Section S4, ESI†) is in good agreement with the DLS analysis shown in Table S1, ESI,† indicating that the gel network does not affect the relaxation behavior of individual (un-jammed) aggregates.

For polymer gels, Shibayama *et al.*[49,53,57] have proposed four different criteria to identify the gel point in DLS experiments.

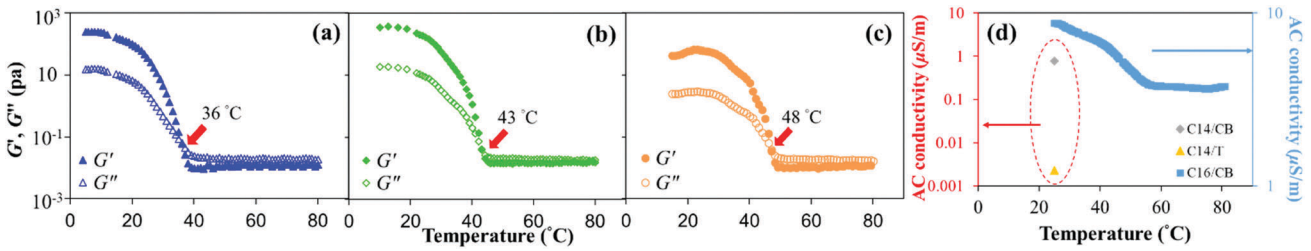

Fig. 3 Dynamic modulus responses upon heating the Hw-pBTTT-C_{16}/CB gels that have been incubated for 24 h at three different temperatures: (a) 5, (b) 10, and (c) 15 °C. The gelation temperature (T_{Gel}) is defined as the crossover of the storage (G') and loss (G'') modulus, as indicated by the arrow in each case. (d) The ac conductivity upon heating the Hw-pBTTT-C_{16}/CB gel (symbol line), as compared with the results for the pBTTT-C_{14}/CB and pBTTT-C_{14}/T solutions (symbol points) at 25 °C and 10 mg mL^{-1}.

Published on 10 January 2018. Downloaded by National Synchrotron Radiation Research on 1/21/2019 4:00:38 AM.

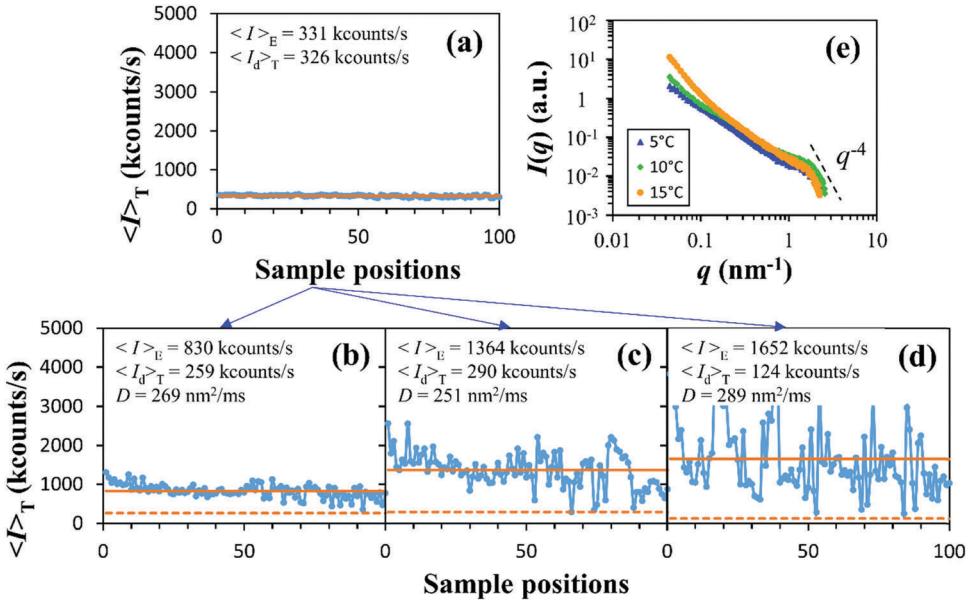

Fig. 4 Sample-position dependences of time-averaged scattering intensity, $\langle I \rangle_T$, at the scattering angle of 90° for (a) Hw-pBTTT-C_{16}/CB solution at 80 °C and the gels incubated at (b) 5, (c) 10, and (d) 15 °C. In each case, the horizontal dashed and solid lines represent, respectively, the value of $\langle I_d \rangle_T$ in comparison with $\langle I \rangle_E$, which is defined as $\sum \langle I \rangle_{T,i} / N$ with N being the total number of randomly chosen sample positions; (e) SAXS profiles for the Hw-pBTTT-C_{16}/CB gels, where the symbols represent the results at three different gelation temperatures: 5 (blue up-triangles), 10 (green diamonds), and 15 °C (orange spheres).

Similar features can be noticed for the investigated Hw-pBTTT-C_{16}/CB, as detailed below. Fig. 5 presents the ICF (intensity correlation function) measured at the scattering angle of 90° upon steadily heating (heating rate = 4 °C min^{-1}) the Hw-pBTTT-C_{16}/CB gel incubated at 15 °C, similar to the condition for Fig. 3. An abrupt drop in the average scattering intensity occurs at a temperature of about 48 °C (see the inset figure), which is in good agreement with T_{Gel} = 48 °C in Fig. 3c. Thus, there is a good agreement between rheological (macroscopic) and light scattering (microscopic) characterizations of the gel point.

Interestingly, the inset figure of Fig. 5 reveals that the gel–sol transition of Hw-pBTTT-C_{16}/CB actually involves four distinct transition states. According to the detailed structural analysis presented later, the major physical events are as follows: the gel structure (incubated at 15 °C) is first broken down upon heating in stage I, when the interconnected (micrometer-sized) clusters are gradually set free, a considerably lower scattering intensity is observed in stage II. The nearly unchanged scattering intensity in stage II involves the decomposition of the aforementioned cluster species that alters the associated relaxation behavior substantially, as we discuss shortly. Passing the gel point at 48 °C, the resulting (smaller) aggregate clusters formed in stage II coexist with their building particles in stage III, followed by a rise in the scattering intensity in stage IV that essentially transforms the (spherical) building particles back to rod-like aggregates for the pristine solution at 80 °C. A detailed classification and nomenclature of various (colloidal) species constituting a gel sample are presented shortly.

The behavior of $g^{(2)}(q,t) - 1$ (ICF) and the associated decay time distribution ($G(\tau)$) during the same process as described above are shown in Fig. 5. Each of the ICF curves is taken within

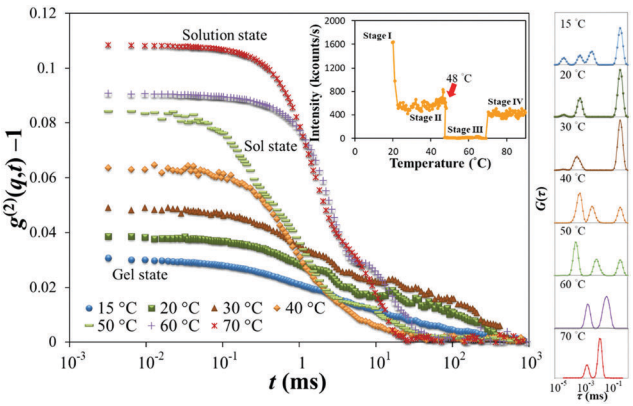

Fig. 5 Temperature dependences of the intensity correlation function (ICF), $g^{(2)}(q,t) - 1$, and the associated decay time distribution (right panels) of Hw-pBTTT-C_{16}/CB that begin with the gel state at 15 °C, followed by steady heating (4 °C min^{-1}). The inset figure shows the corresponding average scattering intensity at θ = 90° during the same heating process.

one minute upon reaching a particular temperature, and therefore the results represent the initial state at a given temperature well. Below 30 °C for the gelation state, the (terminal) decay time of the ICF substantially lengthens, while the corresponding decay time spectrum (right panels) is dominated by the same slow mode (which represents the micrometer-sized clusters) of a large size. As the gel point is approached at ~50 °C, the ICF changes drastically, and the slow mode in the relaxation spectrum wanes and eventually disappears above 70 °C, when the intermediate and fast modes representing the (small) aggregate clusters and building particles, respectively, remain.

 This journal is © The Royal Society of Chemistry 2018

Published on 10 January 2018. Downloaded by National Synchrotron Radiation Research on 1/21/2019 4:00:38 AM.

3.3 Time-evolving DLS features during Hw-pBTTT-C_{16}/CB sol–gel transition

The time evolution of the normalized field autocorrelation function, $|g^{(1)}(q,t)|$, presented in Fig. 6 provides in-depth information on the mechanism and structural features during the Hw-pBTTT-C_{16}/CB sol–gel transition. Detailed analysis of the data, including fits to existing theoretical predictions on polymer and colloid gels, can be found in Section S5, ESI;† the results presented therein may be utilized to estimate, for instance, the mean porosity size (~240 nm) and spatial inhomogeneity length (~20 μm) of the gel network at 15 °C.

At the initial stage of gelation (t = 0 h), the fast and intermediate modes in Fig. 6b correspond to two (diffusive) aggregate species with R_h ~ 10 nm and R_h ~ 100 nm, respectively (R_h being the mean hydrodynamic radius) (see the inset figure in Fig. 6a). In contrast, the slow mode is initially elastic in nature (*i.e.*, $\langle\Gamma\rangle \sim q^0$), and it becomes diffusive (*i.e.*, $\langle\Gamma\rangle \sim q^2$) at a later time t = 8 h. Observing that this particular relaxation mode is determined to represent micrometer-sized clusters in a later SALS analysis, we suggest that this large cluster species formed by the smaller one (*i.e.*, the intermediate mode) initially undertakes aggregation–segregation alternation, which yields an elastic-like response in the DLS analysis. The cluster seems to take shape at a later stage, t = 8 h, when the corresponding SAXS profile (Fig. S8, ESI†) indicates a substantial tightening of the interior structure of the constituting (smaller) aggregate species. Notably, the presently observed alteration from elastic to diffusive attribute for a relaxation mode is unusual in the DLS analysis of polymer gels, yet it seems to be consistent with the rheological responses discussed later. The long-time feature of $|g^{(1)}(q,t)|$ (t = 24 h) also bears some peculiarity not commonly observed for polymer gels; see the discussion in Section S5, ESI.† Thus, the colloidal attributes of the Hw-pBTTT-C_{16}/CB gels should be evident.

In summary, the DLS features during the Hw-pBTTT-C_{16}/CB sol–gel transition render it possible to clearly identify three major (colloidal) aggregate species, classified as the building particle (the fast mode), aggregate cluster (the intermediate mode), and micrometer-sized cluster (the slow mode) in the following (static) scattering analysis, which helps to provide more quantitative information on the geometrical and structural features of individual aggregate species.

3.4 SALS/SLS/SAXS analysis of structural features of Hw-pBTTT-C_{16}/CB sol and gel

Combined scattering intensity profiles, $I(q)$, for the Hw-pBTTT-C_{16}/CB sol and gel utilize measurements from small-angle light scattering (SALS), static (wide-angle) light scattering (SLS), and small-angle X-ray scattering (SAXS) techniques. The combined SALS and SLS profiles are smoothly transited to the SAXS profile through an arbitrary vertical shift. The resulting profiles are presented in Fig. 7, with an overall q range covering length scales of about five orders of magnitude.

We discuss first the SALS and SLS profiles for Hw-pBTTT-C_{16}/CB incubated at the gelation temperature of 15 °C. The results shown in Fig. 7a and b correspond to the initial sol state (at t = 0 h) and the eventual gel state (at t = 24 h), respectively. A salient feature in Fig. 7b for the gel is a distinguishing maximum at $q = q_{max} \approx 3 \times 10^{-4}$ nm^{-1} that is unobserved with the sol in Fig. 7a. Accordingly, a characteristic length $\Lambda = 2\pi/q_{max} \approx 20$ μm is determined, which represents the correlation length for regions of distinct two-phase structures (*i.e.*, polymer-rich or polymer-depleted)—the so-called spatial inhomogeneity length in early studies; see also the OM image and pictorial illustrations in Fig. 8. Besides this iconic structural feature, the SALS profile at low q provides a way to estimate the size of the micrometer-sized clusters using the Guinier plot (see the results in Table 1). In contrast, the

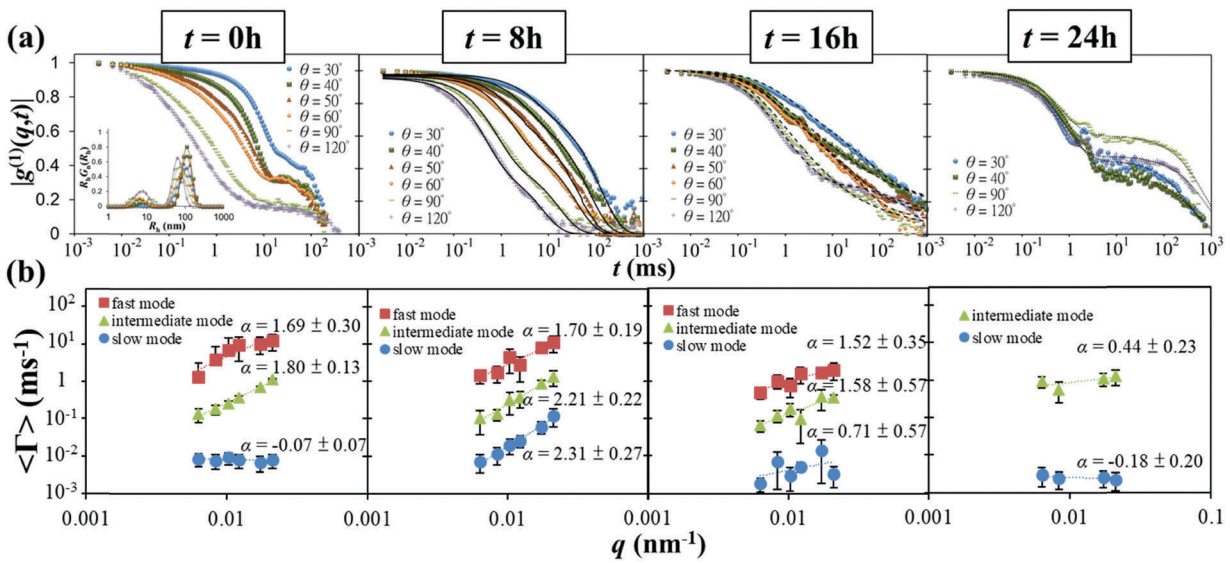

Fig. 6 Time evolutions of (a) the angular dependence of the field autocorrelation function, $|g^{(1)}(q,t)|$, and (b) the corresponding decay rate ($\langle\Gamma\rangle$) as a function of the scattering vector q for the Hw-pBTTT-C_{16}/CB sol–gel transition at 15 °C. Some of the data in (a) are fitted using eqn (S2) (solid lines), (S3) (dashed lines), and (S4) (dotted line), ESI.†

Published on 10 January 2018. Downloaded by National Synchrotron Radiation Research on 1/21/2019 4:00:38 AM.

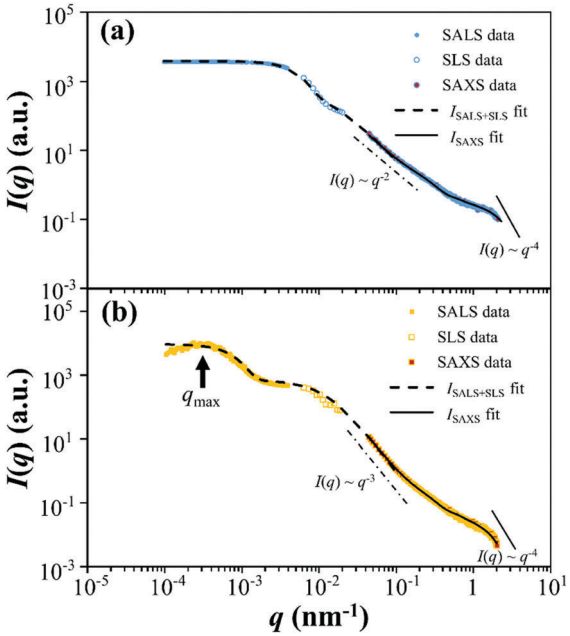

Fig. 7 Combined SALS, SLS, and SAXS intensity profiles for Hw-pBTTT-C_{16}/CB (a) sol (T = 15 °C, t = 0 h) and (b) gel (T = 15 °C, t = 24 h). At low q, $I_{SALS}(q)$ + $I_{SLS}(q)$ data along with the low-q part of $I_{SAXS}(q)$ (for $q < 0.15$ nm^{-1}) are described by eqn (S8) and (S9) (ESI†) (dashed line); at higher q (for $q > 0.15$ nm^{-1}), the solid line represents the fit of the remaining $I_{SAXS}(q)$ data using eqn (S10), ESI.†

corresponding SALS profile is literally flat for the sol in Fig. 7a, indicating the absence of micrometer-sized clusters.

At still higher q, the SALS profile for the gel exhibits a pronounced plateau, followed by the SLS profile that displays the scattering behavior of $I(q) \sim q^{-2}$ for both sol and gel. Thus, the SLS data should reflect the geometrical features of the aggregate clusters that constitute the micrometer-sized clusters above, as well as their interior structure forged by the (smaller) building particles. Accordingly, the SALS and SLS data in this region, along with an extended low-q part of SAXS data (approximately, $q < 0.1$ nm^{-1}), may be described by a combination of Guinier function and structure-plus-form factor; see the expressions in eqn (S8) and (S9), ESI.† The fits are presented in Fig. 7a and b (dashed lines), with the material parameters gathered in Table 1.

In turn, the high-q part of the SAXS profile of both sol and gel may be described by the following two contributions: the interior structure of the building particles plus some isolated gelators—the primal packing units of the building particles. In fact, the contribution of gelators in the highest-q region is marked by some slight leveling, as well as a further downturn showing the characteristic scaling behavior of $I(q) \sim q^{-4}$ for spherical gelators. The functional form used for the fitting can be found in eqn (S10), ESI.† The fits are shown by the solid lines in Fig. 7 superimposed on the SAXS data, with the material properties given in Table 1.

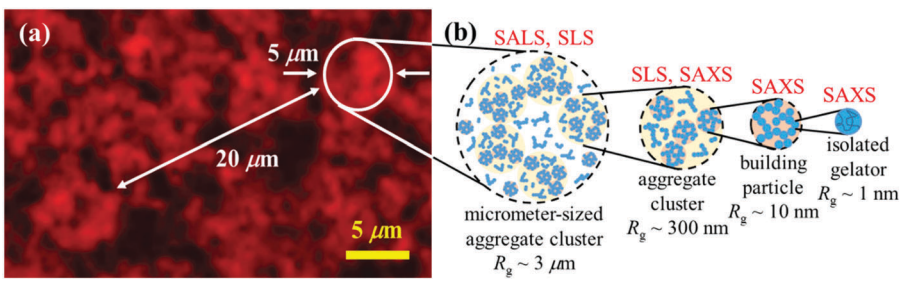

Fig. 8 (a) Thin-film morphology taken from the OM image of the Hw-pBTTT-C_{16}/CB gel incubated at T = 15 °C and t = 24 h; (b) schematic illustrations of hierarchical colloid formation and bridging that underlie the Hw-pBTTT-C_{16}/CB gel network.

Table 1 Material properties extracted from combined SALS/SLS/SAXS analysis of the Hw-pBTTT-C_{16}/CB sol and gel incubated at 15 °C

Methods	Parameters		Sol	Gel
SALS/SLS/SAXS	Micrometer-sized cluster	$I_G(0)$ [a.u.]	—	8674
		Radius of gyration (R_g) [nm]	—	2240
	Aggregate cluster	$I_{G,agg}(0)$ [a.u.]	3335	70
		Radius of gyration ($R_{g,agg}$) [nm]	337	487
		$I_{L,agg}(0)$ [a.u.]	493	634
		Characteristics length (ξ) [nm]	80	72
		Fractal dimension of the network (d_f)	2.1	3.0
		Radius of sphere (R_{bul}) [nm]	10	10
		Radius of gyration $R_{g,agg}_S(q)^a$ [nm]	296	432
	Isolated gelator	$I_{L,iso}(0)$ [a.u.]	4.0	0.6
		Characteristics length (ξ) [nm]	4.8	4.3
		Fractal dimension of the network (d_f)	2.5	3.0
		$I_{P,iso}(0)$ [a.u.]	0.26	0.03
		Radius of sphere (R_{iso}) [nm]	1.0	1.3
		Radius of gyration $R_{g,bul}_S(q)^a$ [nm]	23	26

[a] Calculated from the relation $R_g_S(q) = [d_f(d_f + 1)]^{0.5}\xi$.

 This journal is © The Royal Society of Chemistry 2018

Published on 10 January 2018. Downloaded by National Synchrotron Radiation Research on 1/21/2019 4:00:38 AM.

A noteworthy feature of the low-q SAXS profile is the distinguishing scattering behaviors of $I(q) \sim q^{-2}$ and $I(q) \sim q^{-3}$ for the sol and gel, respectively. The results suggest that the interior structure of the aggregate clusters becomes substantially more compact (*i.e.*, d_f = 2 to 3; see Table 1) as the sol turns into gel (*cf.* $d_f \sim 2.5$ for the building particles with little alteration). This feature might reveal the mechanism by which the micrometer-sized clusters are formed by these aggregate clusters in the gel state, as evidenced by both dynamic (DLS) and static (SALS) analyses. A similar mechanism, in fact, might have driven the mutual bonding between micrometer-sized clusters to form the gel network, akin to the concomitant phase alterations noted previously for the colloidal gel of MEH-PPV fostered in a hybrid solvent medium.[26] Because this "tightening" process occurs within a large aggregate cluster ($R_g \sim 300$ nm), it is curious whether a similar change in local π–π stacking is responsible for this gelation phenomenon. In this respect, we note that the WAXS data at still higher q are ill-resolved and cannot serve the purpose of further discrimination; the UV-vis spectra shown in Fig. S2, ESI† exhibit only a slight red-shift for the gel sample, suggesting (consistently) a more compact aggregate structure without any clear signs of an enhanced π–π stacking.

Overall, the material properties gathered in Table 1 along with previous discussions indicate generally good agreement between dynamic (DLS) (see information in Table S1, ESI†) and static (SALS/SLS/SAXS) analyses on the geometrical and structural features of the three main aggregate species that constitute the Hw-pBTTT-C_{16}/CB sol and gel. Fig. 8b pictorially summarizes the hierarchical colloidal formation and bridging that underlie the Hw-pBTTT-C_{16}/CB gel in this study.

3.5 Rheological properties

Viscoelastic behavior is particularly relevant for a gel, as it helps to reveal the impact of the underlying (multiscale) structural features on the mechanical/processing properties desirable in a practical application. The results of the (oscillatory) strain-sweep and frequency-sweep measurements on the gel samples fostered at three different temperatures (*i.e.*, T = 15, 10, and 5 °C) can be found in Section S7, ESI.† Below, we discuss a representative case from the frequency-sweep measurements on the gelling sample at T = 15 °C to elucidate the general viscoelastic features during the Hw-pBTTT-C_{16}/CB sol–gel transition.

At the initial sol state (t = 0 h), as well as in an early stage of gelation (t = 8 h), Fig. 9 shows that the overall features of G' and G'' differ only slightly. Instead of exhibiting the typical terminal responses, $G' \sim \omega^2$ and $G'' \sim \omega^1$, for polymer solutions, there is a pronounced plateau region at low frequencies, especially for the elastic modulus G'. This viscoelastic feature seems to be customarily associated with solution systems consisting of large aggregate clusters.[58] What appears to be unusual, though, is that G' exceeds G'' at a higher frequency as the gelation proceeds from t = 0 h to t = 8 h. Physically, this implies that the system as a whole becomes more fluid-like, except within local length scales (which correspond to high-frequency responses), where G' lies notably above G''. The opposite trend is often observed during the gelation process, namely, G' becomes dominant at a lower frequency as the gelation proceeds.[59] We suspect that this anomaly of the Hw-pBTTT-C_{16}/CB gel is related to the DLS feature discussed earlier with Fig. 6b for the changing attributes of the slow mode (which is elastic at t = 0 h and turns diffusive at t = 8 h). At still longer gelation times (t = 16 h), the dynamic modulus response resumes the commonplace feature of $G' \gg G''$, with both quantities exhibiting little or no frequency dependence.

Another perspective for interpreting the short and intermediate-time responses of the dynamic modulus of Hw-pBTTT-C_{16}/CB gels is to invoke the notion of critical gels, for which it is not unusual that G' and G'' remain close to each other over a wide range of frequencies.[60] In fact, critical gels represent more a sol state than a real gel, or alternatively, they might be regarded as some kind of "transient gel". Such a transient gelation state may confer sufficient fluidity to a gelling sample for easy processing, while further development of the gel network will eventually make the material elastic in nature. This physical picture is indeed consistent with the results of prior dynamic/static scattering analyses, wherein the Hw-pBTTT-C_{16}/CB gelation has been resolved to undergo various stages of colloidal formation and bridging before the gel network ripens.

For a gelling system, the behavior of the time-dependent complex modulus (G^*) may be utilized to reveal the underlying gelation kinetics. Fig. 10a shows the results of the time-sweep experiment for Hw-pBTTT-C_{16}/CB gels fabricated at three different temperatures. At the lowest gelation temperature, T = 5 °C, the onset of gelation (defined here as the occasion when G^* exhibits an abrupt rise) can be seen to take place within about ten minutes due to the strong driving force that induces gelation. As the temperature increases, the whole gelation process substantially lengthens. Importantly, the results suggest that harder Hw-pBTTT-C_{16}/CB gels may be fostered within reasonably short times (*e.g.*, 1 h), if a lower gelation temperature

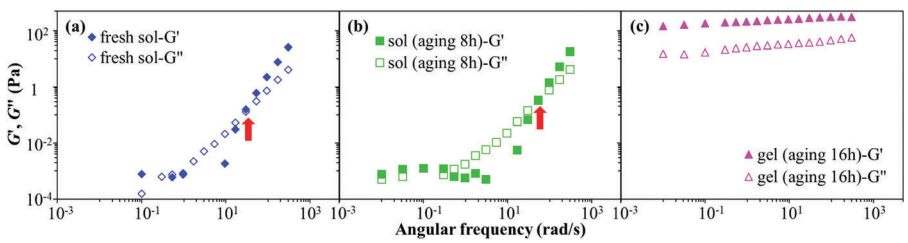

Fig. 9 Storage (G') and loss (G'') modulus as functions of angular frequency for Hw-pBTTT-C_{16}/CB during the gelation process at T = 15 °C: (a) t = 0, (b) t = 8, and (c) t = 16 h. The arrow indicates the crossover point of G' and G''.

Published on 10 January 2018. Downloaded by National Synchrotron Radiation Research on 1/21/2019 4:00:38 AM.

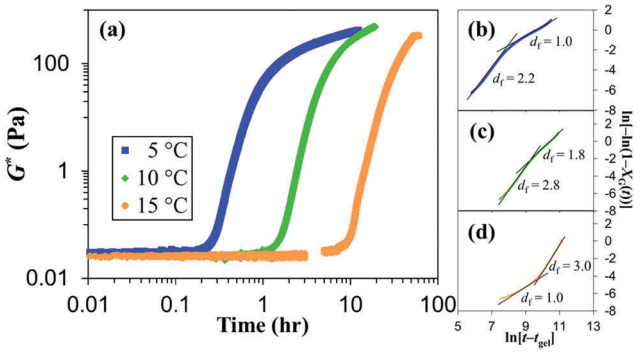

Fig. 10 (a) Complex modulus (G^*) as a function of sweeping time at ω = 10.0 rad s^{-1} for Hw-pBTTT-C_{16}/CB gels incubated at three different temperatures; the corresponding Avrami plots for (b) T = 5, (c) 10, and (d) 15 °C.

is adopted. However, the underlying gel structure varies, too, as we discuss below. It is also worth noting that the imposition of even a small strain during the rheological measurements suffices to somewhat lengthen the overall gelation process, as compared with prior light scattering experiments.

To resolve the gelation kinetics, the model derived by Li and Liu[61] for the Avrami theory of phase changes is employed,[11,15,26] as detailed in Section S7, ESI.† Fig. 10b–d presents the results of the fitting, the slopes in each plot denoting the associated fractal dimensions at various stages of gelation. A common feature is that the slope changes abruptly at certain intermediate times, although the overall trend differs substantially for the three gel systems under investigation. For the gels incubated at lower temperatures, T = 5 and 10 °C, the fractal dimension begins with a larger value and then decreases appreciably in a later stage, whereas the opposite trend is observed for the gel produced at a higher temperature, T = 15 °C. Below, we discuss the physical significance of these phenomena.

By slowing down the gelation process at a higher system temperature, as suggested by the features in Fig. 10a, Hw-pBTTT-C_{16}/CB aggregate clusters would gain more time to properly align themselves and, according to Fig. 10d for T = 15 °C, selectively bridge each other to form 1-D strands (note: another possibility, as suggested by Fig. 6b, is that the 1-D kinetics arises from the aggregation–segregation "reaction" of micrometer-sized clusters at an early stage of gelation), which at a later stage interconnect to form a 3-D gel network. The mutual bonding of micrometer-sized clusters may be regarded as a reaction-limited process in this case, and, consistent with the dynamic modulus responses in Fig. 9, the system initially enjoys sufficient fluidity (when the 1-D bridging or reaction proceeds) and becomes dominantly elastic (when the 3-D bridging prevails) only at a later stage (t > 16 h). In contrast, the gelation at lower temperatures proceeds at a much faster rate initially that is typical of a diffusion-limited process, wherein randomized (3-D) interconnection between nearby clusters quickly results in a more compact gel network and, consequently, a higher mechanical strength. In agreement with these features, the position dependence of the average scattering intensity in Fig. 4b–d clearly reveals a higher degree of ergodicity at lower gelation temperatures, when a relatively homogeneous bulk structure is formed. The prominently nonergodic gel formed at T = 15 °C likely contains a higher void fraction that notably softens the material. In summary, the results shown in Fig. 10 based on the time-sweep dynamic modulus measurements suggest that gelation temperature can have an important impact not only on the kinetic pathway but also on the eventual gel microstructure and mechanical strength, as previously reported for polymeric (conjugated polymer)[15] and colloidal (low-molecular-mass organic gelator) gels.[62]

4. Conclusions

A benchmark Hw-pBTTT-C_{16}/CB solution (10 mg mL^{-1}) has been shown to form gels through a peculiar pathway of hierarchical colloidal bridging, as the system temperature was reduced from T = 80 °C for the pristine solution (when the building particles assume an anisotropic, rod-like shape) to three different gelation temperatures, T = 5, 10, and 15 °C (when the building particles turn spherical in shape); the building particles (~10 nm in mean radius) were later analyzed through SAXS data to be composed of smaller spherical gelators (~1 nm). The building particle (~10 nm), aggregate cluster (~300 nm), and micrometer-sized cluster (~3 μm) were shown to be formed by hierarchical colloidal bridging, with the last species eventually interconnecting to form the gel network (with mean porosity size ~240 nm and spatial inhomogeneity length ~20 μm at T = 15 °C) after about one-day aging. Rheological measurements and detailed kinetic analysis of time-sweep dynamic modulus data suggested that in addition to varying gelation rate and mechanical strength, the gelation temperature can have a notable impact on the initial colloidal packing which, for instance, results in a prominently nonergodic and porous structure for the soft gel incubated at a higher temperature T = 15 °C. The exact (local) structural alteration that triggered the series of events, including a substantial tightening of aggregate cluster interiors which, in turn, fosters the micrometer-sized clusters pivotal for the eventual gel network, remains enigmatic and should be left to future exploration.

In a practical assessment, the ac conductivity of pBTTT-C_{16}/CB was found to exhibit a notable upturn near the gelation temperature, well above those achieved by the counterpart pBTTT-C_{14} solutions (in chlorobenzene or toluene) which, in interesting contrast, cannot be brought to the gel phase under similar experimental conditions. The disparities might, in part, be ascribed to the improved solvation of pBTTT-C_{16} having longer side-group units, thus allowing for the formation of large yet loose aggregate clusters upon fast quenching without exhibiting macroscopic precipitation as has been observed for pBTTT-C_{14} solutions. In a future perspective, it is worth pursuing these unresolved issues while exploring further the versatile features and applications of pBTTT-C_{16} solutions and gels.

Conflicts of interest

There are no conflicts of interest to declare.

This journal is © The Royal Society of Chemistry 2018

Published on 10 January 2018. Downloaded by National Synchrotron Radiation Research on 1/21/2019 4:00:38 AM.

Acknowledgements

This research was supported by the Ministry of Science and Technology of ROC (MOST 103-2221-E-194-059-MY3). We acknowledge the NSRRC of ROC for providing beamtimes and facilitating the SAXS experiments.

References

1 S. Günes, H. Neugebauer and N. S. Sariciftci, *Chem. Rev.*, 2007, **107**, 1324–1338.
2 K. M. Coakley and M. D. McGehee, *Chem. Mater.*, 2004, **16**, 4533–4542.
3 J. Burroughes, D. Bradley, A. Brown, R. Marks, K. Mackay, R. Friend, P. Burns and A. Holmes, *Nature*, 1990, **347**, 539–541.
4 R. H. Friend, R. W. Gymer, A. B. Holmes, J. H. Burroughes, R. N. Marks, C. Taliani, D. D. C. Bradley, D. A. Does Santos, J. L. Bredas, M. Logdlund and W. R. Salaneck, *Nature*, 1999, **397**, 121–128.
5 C. D. Dimitrakopoulos and P. R. L. Malenfant, *Adv. Mater.*, 2002, **14**, 99–117.
6 A. R. Murphy and J. M. J. Fréchet, *Chem. Rev.*, 2007, **107**, 1066–1096.
7 D. T. McQuade, A. E. Pullen and T. M. Swager, *Chem. Rev.*, 2000, **100**, 2537–2574.
8 U. Lange, N. V. Roznyatovskaya and V. M. Mirsky, *Anal. Chim. Acta*, 2008, **614**, 1–26.
9 S. S. Babu, V. K. Praveen and A. Ajayaghosh, *Chem. Rev.*, 2014, **114**, 1973–2129.
10 G. M. Newbloom, K. M. Weigandt and D. C. Pozzo, *Soft Matter*, 2012, **8**, 8854–8864.
11 G. M. Newbloom, K. M. Weigandt and D. C. Pozzo, *Macromolecules*, 2012, **45**, 3452–3462.
12 S. Malik, T. Jana and A. K. Nandi, *Macromolecules*, 2001, **34**, 275–282.
13 G. M. Newbloom, F. S. Kim, S. A. Jenekhe and D. C. Pozzo, *Macromolecules*, 2011, **44**, 3801–3809.
14 M. Koppe, C. J. Brabec, S. Heiml, A. Schausberger, W. Duffy, M. Heeney and I. McCulloch, *Macromolecules*, 2009, **42**, 4661–4666.
15 P. de la Iglesia and D. C. Pozzo, *Soft Matter*, 2013, **9**, 11214–11224.
16 M. J. Sobkowicz, R. L. Jones, R. J. Kline and D. M. DeLongchamp, *Macromolecules*, 2012, **45**, 1046–1055.
17 P.-T. Huang, Y.-S. Chang and C.-W. Chou, *J. Appl. Polym. Sci.*, 2011, **122**, 233–240.
18 B.-G. Kim, E. J. Jeong, H. J. Park, D. Bilby, L. J. Guo and J. Kim, *ACS Appl. Mater. Interfaces*, 2011, **3**, 674–680.
19 W. Xu, H. Tang, H. Lv, J. Li, X. Zhao, H. Li, N. Wang and X. Yang, *Soft Matter*, 2012, **8**, 726–733.
20 C.-Y. Chen, S.-H. Chan, J.-Y. Li, K.-H. Wu, H.-L. Chen, J.-H. Chen, W.-Y. Huang and S.-A. Chen, *Macromolecules*, 2010, **43**, 7305–7311.
21 Z.-Q. Lin, N.-E. Shi, Y.-B. Li, D. Qiu, L. Zhang, J.-Y. Lin, J.-F. Zhao, C. Wang, L.-H. Xie and W. Huang, *J. Phys. Chem. C*, 2011, **115**, 4418–4424.
22 C. C. Kitts and D. A. Vanden Bout, *Polymer*, 2007, **48**, 2322–2330.
23 M. Knaapila and A. P. Monkman, *Adv. Mater.*, 2013, **25**, 1090–1108.
24 J.-H. Chen, C.-S. Chang, Y.-X. Chang, C.-Y. Chen, H.-L. Chen and S.-A. Chen, *Macromolecules*, 2009, **42**, 1306–1314.
25 C.-Y. Chen, C.-S. Chang, S.-W. Huang, J.-H. Chen, H.-L. Chen, C.-I. Su and S.-A. Chen, *Macromolecules*, 2010, **43**, 4346–4354.
26 R. H. Guo, C. H. Hsu, C. C. Hua and S. A. Chen, *J. Phys. Chem. B*, 2015, **119**, 3320–3331.
27 P.-S. Wang, H.-H. Lu, C.-Y. Liu and S.-A. Chen, *Macromolecules*, 2008, **41**, 6500–6504.
28 J.-H. Chen, C.-W. Chiu, L.-C. Chen, S.-Y. Lai and C.-C. Lee, *Polymer*, 2012, **53**, 4843–4854.
29 D. Alcazar, F. Wang, T. M. Swager and E. L. Thomas, *Macromolecules*, 2008, **41**, 9863–9868.
30 S. Ludwigs, *P3HT Revisited-from Molecular Scale to Solar Cell Devices*, Springer, New York, 2015.
31 S. Malik and A. K. Nandi, *J. Appl. Polym. Sci.*, 2007, **103**, 2528–2537.
32 B. H. Hamadani, D. J. Gundlach, I. McCulloch and M. Heeney, *Appl. Phys. Lett.*, 2007, **91**, 243512.
33 I. McCulloch, M. Heeney, C. Bailey, K. Genevicius, I. MacDonald, M. Shkunov, D. Sparrowe, S. Tierney, R. Wagner, W. Zhang, M. L. Chabinyc, R. J. Kline, M. D. McGehee and M. F. Toney, *Nat. Mater.*, 2006, **5**, 328–333.
34 D. M. DeLongchamp, R. J. Kline, Y. Jung, E. K. Lin, D. A. Fischer, D. J. Gundlach, S. K. Cotts, A. J. Moad, L. J. Richter, M. F. Toney, M. Heeney and I. McCulloch, *Macromolecules*, 2008, **41**, 5709–5715.
35 D. M. DeLongchamp, R. J. Kline, E. K. Lin, D. A. Fischer, L. J. Richter, L. A. Lucas, M. Heeney, I. McCulloch and J. E. Northrup, *Adv. Mater.*, 2007, **19**, 833–837.
36 M. L. Chabinyc, M. F. Toney, R. J. Kline, I. McCulloch and M. Heeney, *J. Am. Chem. Soc.*, 2007, **129**, 3226–3237.
37 J. K. Lee, W. L. Ma, C. J. Brabec, J. Yuen, J. S. Moon, J. Y. Kim, K. Lee, G. C. Bazan and A. J. Heeger, *J. Am. Chem. Soc.*, 2008, **130**, 3619–3623.
38 C. V. Hoven, X.-D. Dang, R. C. Coffin, J. Peet, T.-Q. Nguyen and G. C. Bazan, *Adv. Mater.*, 2010, **22**, E63–E66.
39 J. A. Merlo and C. D. Frisbie, *J. Polym. Sci., Part B: Polym. Phys.*, 2003, **41**, 2674–2680.
40 R. J. Kline, D. M. DeLongchamp, D. A. Fischer, E. K. Lin, L. J. Richter, M. L. Chabinyc, M. F. Toney, M. Heeney and I. McCulloch, *Macromolecules*, 2007, **40**, 7960–7965.
41 D. M. DeLongchamp, R. J. Kline, Y. Jung, D. S. Germack, E. K. Lin, A. J. Moad, L. J. Richter, M. F. Toney, M. Heeney and I. McCulloch, *ACS Nano*, 2009, **3**, 780–787.
42 P. Brocorens, A. Van Vooren, M. L. Chabinyc, M. F. Toney, M. Shkunov, M. Heeney, I. McCulloch, J. Cornil and R. Lazzaroni, *Adv. Mater.*, 2009, **21**, 1193–1198.
43 E. Cho, C. Risko, D. Kim, R. Gysel, N. Cates Miller, D. W. Breiby, M. D. McGehee, M. F. Toney, R. J. Kline and J.-L. Bredas, *J. Am. Chem. Soc.*, 2012, **134**, 6177–6190.
44 J. E. Northrup, *Phys. Rev. B: Condens. Matter Mater. Phys.*, 2007, **76**, 245202.
45 Q. Sun, K. Park and L. Dai, *J. Phys. Chem. C*, 2009, **113**, 7892–7897.

Published on 10 January 2018. Downloaded by National Synchrotron Radiation Research on 1/21/2019 4:00:38 AM.

46 H. L. Yi, C. H. Wu, C. I. Wang and C. C. Hua, *Macromolecules*, 2017, **50**, 5498–5509.
47 Y. H. Wen, P. C. Lin, C. C. Hua and S. A. Chen, *J. Phys. Chem. B*, 2011, **115**, 14369–14380.
48 S. Wang, J.-C. Tang, L.-H. Zhao, R.-Q. Png, L.-Y. Wong, P.-J. Chia, H. S. O. Chan, P. K.-H. Ho and L.-L. Chua, *Appl. Phys. Lett.*, 2008, **93**, 162103.
49 S. Mitsuhiro, *Bull. Chem. Soc. Jpn.*, 2006, **79**, 1799–1819.
50 P. Terech and R. G. Weiss, *Chem. Rev.*, 1997, **97**, 3133–3160.
51 Y. Zhao, G. Zhang and C. Wu, *Macromolecules*, 2001, **34**, 7804–7808.
52 M. Shibayama, T. Norisuye and S. Nomura, *Macromolecules*, 1996, **29**, 8746–8750.
53 S. Mitsuhiro and N. Tomohisa, *Bull. Chem. Soc. Jpn.*, 2002, **75**, 641–659.
54 S. Seiffert, *Polym. Chem.*, 2017, **8**, 4472–4487.
55 F. Di Lorenzo and S. Seiffert, *Polym. Chem.*, 2015, **6**, 5515–5528.
56 M. Kroon, G. H. Wegdam and R. Sprik, *Phys. Rev. E: Stat. Phys., Plasmas, Fluids, Relat. Interdiscip. Top.*, 1996, **54**, 6541–6550.
57 M. Shibayama, S. Takata and T. Norisuye, *Phys. A*, 1998, **249**, 245–252.
58 N. Yang, J. L. Hutter and J. R. de Bruyn, *J. Rheol.*, 2013, **57**, 1739–1759.
59 K. Nishinari, Some Thoughts on The Definition of a Gel, *Gels: Structures, Properties, and Functions: Fundamentals and Applications*, Springer, Berlin/Heidelberg, 2009, vol. 136, pp. 87–94.
60 H. H. Winter and F. Chambon, *J. Rheol.*, 1986, **30**, 367–382.
61 J.-L. Li and X.-Y. Liu, *Adv. Funct. Mater.*, 2010, **20**, 3196–3216.
62 R. Lam, L. Quaroni, T. Pedersen and M. A. Rogers, *Soft Matter*, 2010, **6**, 404–408.

 This journal is © The Royal Society of Chemistry 2018